

A Generic Crystallization-like Model That Describes the Kinetics of Amyloid Fibril Formation^{*[S]♦}

Received for publication, April 24, 2012, and in revised form, June 15, 2012. Published, JBC Papers in Press, July 5, 2012, DOI 10.1074/jbc.M112.375345

Rosa Crespo[‡], Fernando A. Rocha[‡], Ana M. Damas^{§¶}, and Pedro M. Martins^{‡§¶1}

From the [‡]LEPAE, Laboratório de Engenharia de Processos Ambiente e Energia, Departamento de Engenharia Química, Faculdade de Engenharia, Universidade do Porto, 4200-465 Porto, [§]Instituto de Ciências Biomédicas Abel Salazar (ICBAS), Universidade do Porto, 4050-313 Porto, and the [¶]Instituto de Biologia Molecular e Celular (IBMC), Universidade do Porto, 4150-180 Porto, Portugal

Background: Amyloid fibrils are protein aggregates associated with numerous neurodegenerative diseases.

Results: A theoretically consistent, two-parameter model is proposed describing very distinct amyloid fibrillization kinetics.

Conclusion: Amyloid fibril formation takes place by a general mechanism involving supersaturation-dependent nucleation and growth steps.

Significance: This mathematically simple model is expected to be routinely used to characterize the action of new targets for disease therapeutics.

Associated with neurodegenerative disorders such as Alzheimer, Parkinson, or prion diseases, the conversion of soluble proteins into amyloid fibrils remains poorly understood. Extensive “*in vitro*” measurements of protein aggregation kinetics have been reported, but no consensus mechanism has emerged until now. This contribution aims at overcoming this gap by proposing a theoretically consistent crystallization-like model (CLM) that is able to describe the classic types of amyloid fibrillization kinetics identified in our literature survey. Amyloid conversion represented as a function of time is shown to follow different curve shapes, ranging from sigmoidal to hyperbolic, according to the relative importance of the nucleation and growth steps. Using the CLM, apparently unrelated data are deconvoluted into generic mechanistic information integrating the combined influence of seeding, nucleation, growth, and fibril breakage events. It is notable that this complex assembly of interdependent events is ultimately reduced to a mathematically simple model, whose two parameters can be determined by little more than visual inspection. The good fitting results obtained for all cases confirm the CLM as a good approximation to the generalized underlying principle governing amyloid fibrillization. A perspective is presented on possible applications of the CLM during the development of new targets for amyloid disease therapeutics.

Amyloid fibrils are insoluble ordered structures sharing a common cross β -sheet conformation and formed by misassembly of soluble proteins and peptides (1–3). Because these protein aggregates are associated with numerous neurodegenerative diseases, a great deal of effort has been put into understanding the mechanisms of amyloid fibril formation

(4–6). Several biophysical methods have been developed to measure the kinetics of protein aggregation “*in vitro*” (7–11). Thioflavin-T binding fluorescence (12) and turbidity measurements (13) are among the most widely adopted techniques. Despite the limitations of the classical methods (14), they provide quantitative information about the mass increase of amyloid fibrils with time. Typically, the progress of fibrillization is expressed as the normalized fraction of amyloid protein converted into fibrils (α); on a mass basis, α corresponds to the quotient of the fibril mass increase Δm at a given instant divided by the total mass of fibrils formed at the end of the assay Δm_T .

$$\alpha = \frac{\Delta m}{\Delta m_T} \quad (\text{Eq. 1})$$

The time-course results represented in Fig. 1 exemplify well two types of kinetics usually observed during amyloid fibril formation. The sigmoidal $\alpha(t)$ trend obtained for β_2 -microglobulin (β_2m)² (15) (*open symbols*) is characteristic of nucleation-dependent polymerization; an initial lag phase is followed by a phase of rapid growth and then by a stationary phase (16, 17). The hyperbolic shape obtained for transthyretin (*closed symbols*) is more frequently found during seeded aggregation, *i.e.* when an aliquot of solution containing preformed fibrils is added to the amyloidogenic solution to bypass the thermodynamically unfavorable nucleation step (8, 17, 18). Nevertheless, as shown by this example, the absence of a lag phase is also reported for unseeded reactions (18, 19). Between the classical sigmoidal kinetics, showing an inflection point at $\alpha_i = 0.5$, and the hyperbolic/seeded polymerization kinetics, showing no evident inflection point, there are a number of intermediate possibilities that have been comprehensively reviewed by Finke and co-workers (4, 20). As discussed in those reviews, the meaning of the different shapes has been interpreted over the last 50 years according to several thermodynamic and kinetic mechanisms. Given the complexity and variability of the protein aggregation models, a modular approach was recently pro-

* This work was supported by Project PTDC/BIA-PRO/101260/2008 from the Fundação para a Ciência e a Tecnologia, Portugal.

♦ This article was selected as a Paper of the Week.

[S] This article contains supplemental Tables S1 and S2 and Fig. S1.

¹ To whom correspondence should be addressed: Instituto de Ciências Biomédicas Abel Salazar (ICBAS), Universidade do Porto, Rua de Jorge Viterbo Ferreira no. 228, 4050-313 Porto, Portugal. Tel.: 351-222062287; Fax: 351-222062232; E-mail: pmmartins@icbas.up.pt.

² The abbreviations used are: β_2m , β_2 -microglobulin; CLM, crystallization-like model; M-TTR, monomeric transthyretin.

Protein Aggregation Described by a Two-parameter Model

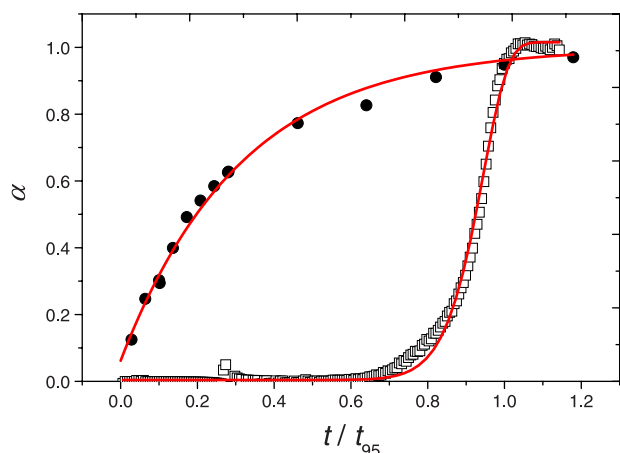


FIGURE 1. Time-dependent normalized fluorescence signal representing typical sigmoidal (open symbols) and hyperbolic (closed symbols) aggregation kinetics of amyloid proteins during amyloidogenesis. For visual clarity, trend lines are represented, and the time axis is normalized by the time for 95% conversion (t_{95}) for each case. Open symbols correspond to the experimental data obtained by Xue *et al.* (15) using $61 \mu\text{M} \beta_2\text{m}$; $t_{95} = 15.6 \text{ h}$. Closed symbols represent continuous fluorescence data from Hurshman *et al.* (18) obtained for 0.15 mg/ml M-TTR , which we digitized into periodic data and normalized by the end-point signal; $t_{95} = 23.4 \text{ s}$.

posed to systematically identify the mechanism that best describes nucleation (or prepolymerization), growth (or polymerization), and fragmentation steps (15). The available fundamental models are in general highly specific for the amyloid polypeptide under study. Models containing a high number of parameters cannot fit to experimental data in a unique way, whereas some of the theoretical elementary steps refer to time frames that are experimentally inaccessible. Overparameterization makes it hard to validate different parts of mechanistically elaborated models (21), which is recognized as a problem in protein aggregation modeling (22). In the pursuit of a consensual, two-parameter model for describing protein aggregation kinetics, the 1997 Finke-Watzky mechanism for transition-metal nanocluster formation (23) was successfully applied to a wide range of kinetic data (4, 20). In the formulation of the Finke-Watzky model, slow continuous nucleation is followed by autocatalytic surface growth so that the overall rate of protein concentration decrease is given by

$$-\frac{dC}{dt} = k_1C + k_2C(C_0 - C) \quad (\text{Eq. 2})$$

with k_1 and k_2 being, respectively, the nucleation and growth average rate constants. For an initial protein concentration C_0 , the solution of the ordinary differential equation can be expressed as

$$\frac{C_0 - C}{C_0} = 1 - \frac{1 + \frac{k_1}{k_2C_0}}{1 + \frac{k_1}{k_2C_0} \exp\left\{\left(1 + \frac{k_1}{k_2C_0}\right)k_2C_0t\right\}} \quad (\text{Eq. 3})$$

Note that the difference ($C_0 - C$) corresponds, by mass balance, to the instantaneous concentration of protein aggregates (20). The Finke-Watzky equation is interconvertible by algebraic manipulation into the Saitô and co-workers equation (24) and into the

equation of Fernández *et al.* (25), which, however, depart from different mechanistic assumptions (see supplemental Table S1). When the nucleation rates are very low ($k_1 \rightarrow 0$), Equation 2 reduces to the differential form of the logistic function, which is commonly used to fit sigmoidal aggregation data (4, 16). Ferrone's equation (26) is another example of a two-parameter protein aggregation model available in literature that predicts the monomer concentration to decrease with the square of time. Although avoiding overparameterization, these models are very useful from a practical point of view, although some simplifying hypothesis adopted during their derivation may lack solid biophysical basis. For example, Saitô and co-workers (24) and Fernández *et al.* (25) describe elementary kinetic steps by reaction-like rate equations that are first-order in relation to the fractional conversion of monomers into fibrils expressed as α and/or $(1 - \alpha)$. In an alternative formalism, Finke and co-workers consider (4, 27) the fibrillar state as the autocatalytic, polymeric form of the protein and express the elementary rate laws as a function of the protein concentrations in the solubilized and aggregated forms. Although theoretically more appropriate, the Finke-Watzky formalism results in the paradox that according to Equation 2, all the dissolved protein is expected to convert into fibrils, *i.e.* the expected steady-state concentration is $C_\infty = 0$. This is not possible in the light of the general phase equilibrium condition and is not supported by measurements of dissolved protein concentration after long incubation times (18, 28, 29). Finally, the applicability of Ferrone's quadratic equation is inherently limited to the early data points corresponding to ~ 10 – 20% of total monomer loss (22).

Kinetic modeling of amyloid fibrillization reactions has also been performed using empirical equations such as linear and exponential decay functions (30). As recently pointed out by Auer and Kashchiev (31) while discussing the applicability of the Avrami equation, it does not seem coincidental that such mathematically simple models are able to describe the $\alpha(t)$ dependence for a wide range of polypeptides and amyloidogenic conditions. With the present contribution, we seek the general principle that seems to govern the kinetics of protein aggregation. We intend to do it in a theoretically consistent way that does not compromise the final simplicity of the model nor its quantitative usefulness. An infinite number of parameter combinations producing equally good agreement with the data should be avoided; that is to say, all the dynamic state variables shall be condensed in a two-parameter model that can be uniquely fit to protein aggregation kinetics. Then, the deepest meaning of each constant should be possible to be determined by using different types of experimental data. For this mechanistic refinement to be possible, oversimplified hypothesis such as those identified in our literature survey should also be avoided during the derivation of the model.

THEORY

Resemblances between amyloid fibril formation and protein crystallization have long been recognized (17). Both processes involve the thermodynamic equilibrium between phases, an initial assembly of macromolecules into stable nuclei (nucleation step), and the subsequent formation of supramolecular structures by the successive addition of growth units (growth or

elongation step). We propose now to quantitatively describe the aggregation kinetics of amyloid proteins using fundamental principles that are familiar to crystal growth scientists.

Thermodynamic Driving Force—We will start by defining the thermodynamic driving force for amyloid fibril formation as the variation in chemical potential $\Delta\mu$ occurring when protein molecules in a supersaturated amyloid solution at temperature T are transferred to a fibrillar state

$$\Delta\mu = kT \ln \frac{a}{a^*} \quad (\text{Eq. 4})$$

where k is the Boltzmann constant and a and a^* are the activities of supersaturated and saturated amyloid solutions. This is analogous to the definition of supersaturation adopted in crystallization from solution (32). Accurate activity coefficients are difficult to obtain for highly nonideal concentrated solutions. For this reason, and for mathematical simplicity, we will define an approximate amyloid supersaturation σ as a function of protein concentration C and protein solubility C^*

$$\sigma = \frac{C - C^*}{C^*} \quad (\text{Eq. 5})$$

The protein solubility corresponds to the concentration of dissolved protein that equilibrates the chemical potential of the insoluble fibrillar phase. In principle, C^* is independent of the initial protein concentration and can be obtained from the remaining concentration of the polypeptide in solution after long reaction times (18). Nevertheless, when measuring protein aggregation in the presence of high macromolecular content (“macromolecular crowding”), volume-excluding effects may lead to different protein concentrations in equilibrium (33). We will return to this issue while discussing possible deviations from the CLM. The total amount of aggregates produced per unit of volume of solution $\Delta m_T/V$ is given by the difference between the mass concentrations C_0 and C^* . Equation 5 can thus be rewritten to express amyloid supersaturation as a function of the fraction of protein converted into amyloid aggregates (α) and of the initial supersaturation (σ_0).

$$\sigma = \frac{(C_0 - C^*) - (C_0 - C)}{C^*} = \frac{\Delta m_T}{VC^*} (1 - \alpha) = \sigma_0 (1 - \alpha) \quad (\text{Eq. 6})$$

Nucleation Step—The mechanism leading to the formation of amyloid nuclei generally includes conformational changes of the native state (34) and different intermediate structures such as polymorphous and oligomeric aggregates (35, 36), whose nature and importance vary from protein to protein (4, 15). Although all of the transitions involve energy barriers of different magnitudes, we will consider that the rate-limiting step is the formation of a critical-sized amyloid nucleus. This postulation finds support in the well known fact that the addition of preformed fibrils to amyloidogenic solutions (seeding) completely eliminates the lag phase and induces immediate fibril formation. Classical nucleation theory (37, 38), based on which numerous phase transition phenomena occurring in nature and technology have been explained (39), will be used to estimate

the frequency at which new fibrils are created. It is admitted that fluctuations in phase density give rise to the appearance of embryonic formations or nuclei that reduce the bulk free energy (due to the variation in chemical potential $\Delta\mu$) and increase the surface free energy (due to the creation of a fibril/solution interface). Above a critical nucleus size, the process spontaneously evolves in the direction of amyloid fibril formation. Recently (38), the following expression was proposed for the critical number of monomeric peptides constituting the amyloid nucleus

$$n^* = \frac{\nu}{\Delta\mu^2} + 1 \quad (\text{Eq. 7})$$

where ν is a constant accounting for the dimensions and interfacial energies of the nanosized fibril. In the same work, the nucleation rate J was expressed as a complex function of the thermodynamic driving force for amyloid fibril formation (38). We will adopt a simplified version of this relationship that takes into account the very high supersaturation levels associated with amyloidogenic conditions (18, 28, 29). For C/C^* ratios much higher than 10, the equilibrium concentration of fibril nuclei is expected to increase linearly with C , greatly simplifying the expression of J to a second-order rate equation

$$J \cong A\sigma^2 \quad (\text{Eq. 8})$$

with A being a σ -independent kinetic factor expressed in units of frequency per solution volume.

Growth Step—During this step, preformed fibrils grow by the successive addition of new structural units. Due to the existence of a preliminary fibril template, the growth (or elongation) step is thermodynamically favored over nucleation; although both processes co-exist during the early phases of incubation (16), fibril elongation is expected to become increasingly predominant (40). Advanced microscopy techniques show indefinite evidences of unidirectional (41–44) and bidirectional amyloid fibril growth (45, 46), reportedly involving intertwining of amyloid filaments and protofibrils (47). Whatever the mechanisms of assembly admitted to occur, phase transition during this step is mostly determined by a secondary nucleation process taking place on the surface of the protein aggregates (44, 48). Therefore, the elongation rate G is proportional to the frequency at which protein molecules leave the solution phase and reach the fibril surface. As previously stated by us for the case of crystal growth from solution (49–51), the attachment probability linearly increases with (i) supersaturation σ , which drives the diffusion of molecules toward the interface; and with (ii) the number of energetically favorable sites for integration. The later quantity was found to be proportional to crystal size during crystallization (49) and is here assumed to be proportional to the length of amyloid fibrils L or, more specifically, to the number of β -sheets constituting the solid phase. We depart from a nonactive binding mechanism, where the lateral binding of monomers is seen as a dynamic reservoir for their subsequent incorporation at both ends of the fibrils (52, 53) (Fig. 2). We further assume that surface adsorption is a reversible process followed by a fast surface diffusion step, which is not rate-limiting while monomers are being recruited into the active sites.

Protein Aggregation Described by a Two-parameter Model

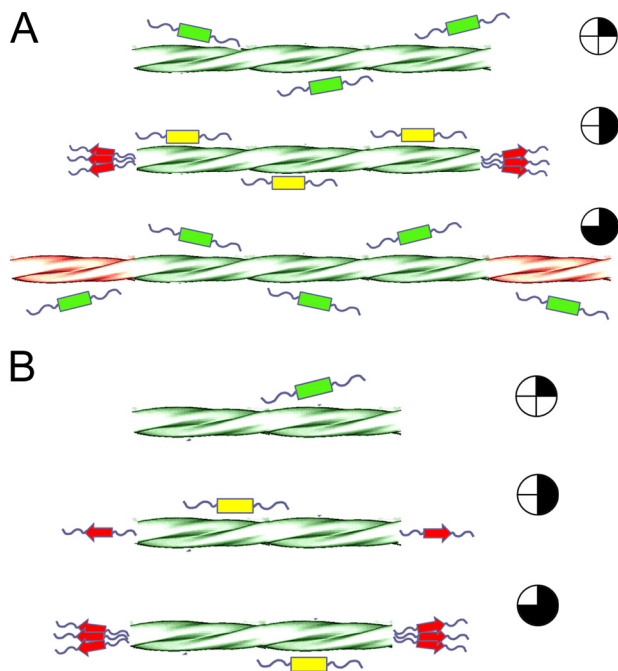


FIGURE 2. Schematic representation of size-dependent amyloid fibril growth. Monomers in solution (green rectangles) diffuse into the surface of fibrils, where they get reversibly adsorbed (yellow rectangles) and rapidly migrate to the fibril ends. Accumulation of adsorbed molecules at the active sites (red arrows) takes place until reaching the minimal number of monomers required for integration and subsequent regeneration of the fibril end. For β_2m , this number was estimated from pre-steady-state kinetic measurements to be ~ 10 monomers (52). Supported by the nonactive site binding mechanism (52, 53), we further assume that lateral migration of molecules is not rate-limiting so that the influx of monomers directly increases with fibril length as the attachment probability also increases. Accordingly, regeneration events take place faster in long fibrils (A) than in short fibrils (B); time lapse is represented by the blackened clock symbols on the right side. Helical representation of amyloid fibrils is adapted from Ref. 54.

The simplified expression for the rate of fibril elongation is thus given by

$$G = \frac{dL}{dt} = k_g \sigma L \quad (\text{Eq. 9})$$

where k_g is a growth rate constant accounting for the influx of amyloidogenic protein molecules arriving to the fibril ends and undergoing conformational changes upon integration. For the constant cross-section area, the mass of fibrils linearly increases with L . Therefore, size-dependent growth provides a phenomenological explanation for the autocatalytic nature of amyloid protein aggregation (16, 55) and for the semiempirical evidences that the elongation rate is proportional to the mass of fibrils, directly as m -dependent growth (22) or indirectly as α -dependent growth (24) and $(C_0 - C)$ -dependent growth (4, 20). A more subtle consequence arising from Equation 9 is that unless specified otherwise by complementary rate laws, overall elongation rates are affected by the total mass of fibrils present in solution but not by their number. We will return to this point during the derivation of the mathematical model and during the discussion of its limitations.

Mathematical Model—Given the kinetics of nucleation and growth just defined, it is important to know how much and how fast amyloid fibrillization will take place. We will start by defining the mass of polypeptide aggregates, m , in the generic case of

fibril formation using a mass of seeds m_0 and taking into account the fibril size distribution.

$$m = m_0 + \Delta m = a_p \sum_{i=0}^{\infty} n_i L_i \quad (\text{Eq. 10})$$

In the second part of the equation, a_p is the cross-section area multiplied by the mass density of amyloid fibrils, and it is assumed to not change significantly with time; n_i is the number of fibrils with characteristic size L_i . It follows that the rate at which m increases with time is given by

$$\frac{dm}{dt} = a_p \sum_{i=0}^{\infty} \frac{dn_i}{dt} L_i + a_p \sum_{i=0}^{\infty} \frac{dL_i}{dt} n_i \quad (\text{Eq. 11})$$

The first sum term accounts essentially for the formation of new amyloid nuclei containing n^* molecules (Equation 7), which occurs at a nucleation frequency J (Equation 8). The second sum term refers to the size-dependent elongation of fibrils (Equation 9). Fibril breakage, although important for the final size distribution and for pathogenic proliferation (56, 57), is not expected by the CLM to influence the overall kinetics of m increase. On the one hand, fragmentation increases the number of fibrils but not their total mass, so the first sum term of Equation 11 remains constant. On the other hand, provided that the initial mass is the same, a large number of shorter and slow growing fibrils are expected to have the same total mass increase per time unit as fewer and fast growing fibrils. This is due to the condition of size-dependent growth resulting from Equation 9, which implies that the same mass of different sized seeds will induce unvarying fibrillization kinetics. Experiments of amyloid fibril formation of β_2m using small amounts of seeds apparently confirm that short, ultrasonicated fibrils induced “essentially the same kinetics” as less fragmented ones (58). Nevertheless, as higher α_0 fractions are used, fragmented seeds seem to promote the initial fibrillization rates ν_0 (15, 52); more surprisingly, when ultrasounds or mechanical agitation are used during incubation, the overall conversion into amyloid fibrils (expressed in terms of final fluorescence intensity) is markedly affected by the type of agitation (59, 60). From these results, we suggest the existence of a thermodynamic rather than kinetic effect associated with fibril breakage. The effective concentration of protein in solution is likely to be influenced by the total number of monomers remaining captive on the fibril ends (Fig. 2). The bigger the fibril fragmentation, the larger the number of fibril ends, and the greater the effect on the effective concentration in equilibrium. Although it is important in explaining unexpected behaviors, we will not be concerned with changing thermodynamics due to fibril breakage and/or volume-excluding effects at this stage of the CLM development. Equation 11 is therefore rewritten as a function of the kinetics of nucleation and growth

$$\frac{dm}{dt} = A \sigma^2 V n^* \frac{M_r}{N_A} + k_g \sigma \sum_{i=0}^{\infty} a_p n_i L_i \quad (\text{Eq. 12})$$

with M_r being the molecular weight of the amyloid protein and N_A being the Avogadro constant. After recognizing that the

sum term corresponds to the total mass m (Equation 10), and expressing Δm and σ as a function of the extent of amyloid fibril formation α (Equations 1 and 6), one gets

$$\frac{d\alpha}{dt} = k_a(1 - \alpha)[k_b(1 - \alpha) + \alpha + \alpha_0] \quad (\text{Eq. 13})$$

where the σ_0 -dependent constant k_a gives the magnitude of the growth step

$$k_a = k_g\sigma_0 \quad (\text{Eq. 14})$$

and k_b gives the relative nucleation-to-growth magnitude

$$k_b = \frac{A\bar{n}^*M_r}{N_A C^* k_g} \quad (\text{Eq. 15})$$

An average value \bar{n}^* is considered for the number of molecules constituting the amyloid nuclei. Although n^* increases as $\Delta\mu$ (and σ) decreases (Equation 7), the average size of the critical nuclei is assumed for now to be dictated by the initial supersaturation σ_0 . In Equation 13, α_0 corresponds to the mass fraction of seeds ($m_0/\Delta m_T$) and not to the initial amyloid conversion, which is 0 for both seeded and unseeded reactions $\alpha(0) = 0$. The analytical solution of the ordinary differential Equation 13 subject to this initial condition is

$$\alpha = 1 - \frac{1}{\frac{k_b + \alpha_0}{1 + \alpha_0} [\exp[k_a t(1 + \alpha_0)] - 1] + 1} \quad (\text{Eq. 16})$$

which in the case of unseeded reactions simplifies to

$$\alpha = 1 - \frac{1}{k_b [\exp(k_a t) - 1] + 1} \quad (\text{Eq. 17})$$

This equation is a major result of our study. Some of the practical and fundamental applications arising from it will now be discussed using experimental amyloid fibrillization kinetics obtained from the literature. Equation 17 will be fitted to the measured variations of α with time to determine the kinetic constants k_a and k_b . In so doing, the growth and nucleation steps will be quantitatively characterized, which is useful to design and predict different amyloidogenic conditions. When the rates of amyloid fibril formation are available for different initial protein concentrations (and for different σ_0 values), further fundamental insight about amyloid fibrillogenesis is gained by disclosing the meaning of the kinetic constants at the molecular scale. Our future work will address the cases of seeded fibrillization kinetics (Equation 16) in more detail.

RESULTS AND DISCUSSION

The CLM will be tested against experimental data published by Xue *et al.* (15) and Hurshman *et al.* (18) that comprehensively describe unseeded sigmoidal and hyperbolic kinetics. Although different numerical methods can be applied to determine the model parameters k_a and k_b , we propose a simplified strategy that uses the time required to reach 50% of the maximal amplitude (t_{50}) and the aggregation rate at that instant (v_{50}). The theoretical value of the product $k_a t_{50}$ is obtained by setting $\alpha = 0.5$ in Equation 17.

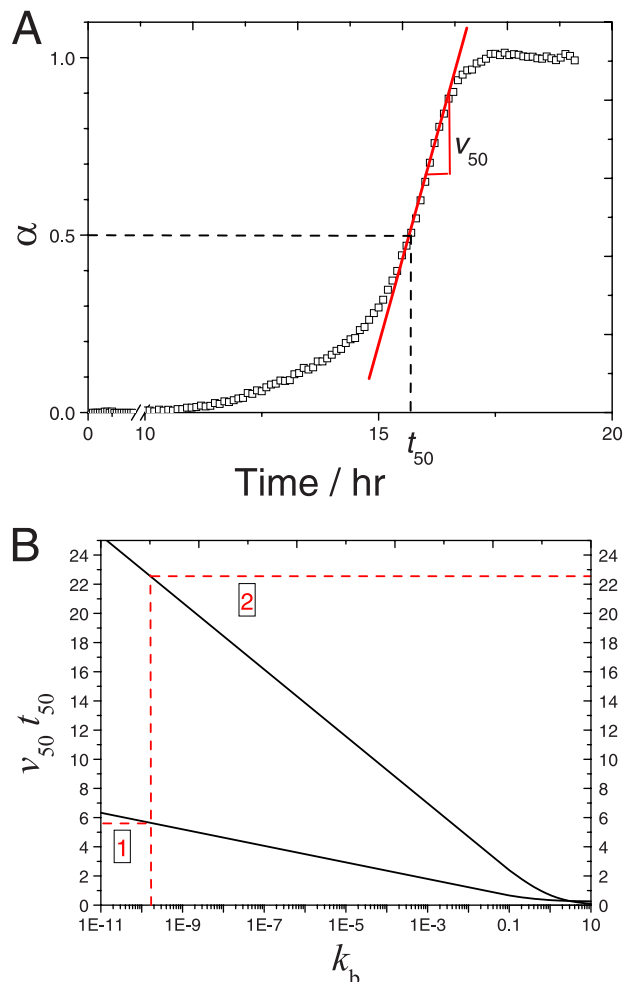


FIGURE 3. Simplified method for determining the kinetic constants k_a and k_b from unseeded amyloid aggregation kinetics. A, illustrative example for determining the time required to reach 50% completion t_{50} (dashed lines) and the aggregation rate at that instant (v_{50}) (solid lines) using the time-dependent, normalized fluorescence signal measured by Xue *et al.* (15) for 61 μM $\beta_2\text{m}$; $t_{50} = 15.6$ h and $v_{50} = 0.36$ h^{-1} . B, the products $v_{50}t_{50}$ (left vertical axis) and $k_a t_{50}$ (right vertical axis) are computed as a function of k_b (log scale) according to Equations 19 and 18, respectively (solid lines). From the kinetic parameters determined in A, k_b is firstly interpolated from the product $v_{50}t_{50}$ and then is used to interpolate the product $k_a t_{50}$, from which k_a is estimated (dashed arrows); $k_b = 1.6 \times 10^{-10}$ and $k_a = 1.44$ h^{-1} .

$$k_a t_{50} = \ln\left(\frac{1}{k_b} + 1\right) \quad (\text{Eq. 18})$$

In the same way, v_{50} corresponds to the derivative given by Equation 13 for $\alpha = 0.5$ and $\alpha_0 = 0$, with the product $v_{50}t_{50}$ also being a sole function of k_b

$$v_{50}t_{50} = \frac{1}{4}(k_b + 1)\ln\left(\frac{1}{k_b} + 1\right) \quad (\text{Eq. 19})$$

As shown in Fig. 3A, v_{50} is obtained from the slope of the experimental $\alpha(t)$ curve at the instant t_{50} . In a first step, the value of k_b is determined from solving Equation 19 using the measured values of t_{50} and v_{50} . The value of k_a is then determined from solving Equation 18 using t_{50} and the k_b constant just estimated. This two-step method for determining the model parameters is graphically illustrated in Fig. 3B. The mechanistic similarities suggested by Fändrich (61) when analyzing 298 amyloid aggre-

Protein Aggregation Described by a Two-parameter Model

gation kinetics of different polypeptides find here their underlying principle. The author noticed that the product of the apparent lag time t_1 and the maximum aggregation rate v_{\max} did not change significantly from an average value of 4.5 with S.D. ± 2.9 (31, 61). Although t_1 is lower than t_{50} , and v_{\max} is greater or equal to v_{50} , the product $t_1 v_{\max}$ is expected to be close to $v_{50} t_{50}$. The representation of Equation 19 in Fig. 3B shows that a relatively narrow range of $v_{50} t_{50}$ values, say between 2 and 6, corresponds to k_b values that vary many orders of magnitude, from $\sim 10^{-11}$ to $\sim 10^{-4}$. That is to say, according to the CLM, very different nucleation-to-growth ratios exhibited by amyloid polypeptides correspond to nearly invariable $v_{50} t_{50}$ and $t_1 v_{\max}$ products. The bad news is that even small experimental errors during aggregation kinetics measurement can lead to great uncertainty on the estimated value of k_b . The values of k_b associated with the $t_1 v_{\max}$ products identified by Fändrich (61) are much lower than 1, so in Equation 19, $k_b + 1 \approx 1$. By combining Equation 18 and the simplified version of Equation 19, one finds that $k_a \approx 4v_{50}$ for the large number of amyloid aggregation kinetics analyzed. The simplified method illustrated in Fig. 3 was applied to more than 200 fibrillization progress curves measured by Xue *et al.* (15) at concentrations of β_2m monomer ranging from 8 to 244 μM . The selection of fitting results given in Fig. 4A illustrates the good agreement obtained throughout the different polymerization stages and for all concentrations. This is especially relevant if one recalls that half-life coordinates (t_{50} and v_{50}) were the only information used to compute the theoretical curves in their full extent. According to Equation 14, the values of k_a should increase linearly with the initial supersaturation level σ_0 . Mean k_a values of replicate experiments are represented in Fig. 4B as a function of the σ_0 values calculated using Equation 5 and a C^* estimation of 0.67 μM for β_2m under acidic conditions (62). The fact that the $k_a(\sigma_0)$ relationship is closer to a power law function than to a linear function is not discouraging. On the contrary, it reflects the increasing diffusional limitations as the C_0 increases from 8 to 244 μM . More concentrated protein solutions result in a higher quantity of suspended fibrils, which in turn decreases the mass transfer rates and does not let k_a increase with σ_0 as fast as in diluted solutions. Concerning the determination of the constant k_b , a great variability of results was obtained for each β_2m concentration that was analyzed. The 95% confidence intervals for the mean k_b included the value 0 in all cases except for $C_0 = 43.7 \mu\text{M}$. The difficulty in finding statistically valid k_b estimations confirms our concerns about the high sensitivity of this parameter, at least in the region of Fig. 3B corresponding to high values of $v_{50} t_{50}$. The same uncertainty does not let us conclude about the meaning of some misfit occurring when α starts to increase using less concentrated β_2m solutions (Fig. 4A). These discrepancies, which were not reproducibly observed, may represent different nucleation rates from those considered by the CLM or, more simply, may result from experimental base-line variations that are more likely to occur during slower fibrillization kinetics.

So far we have been analyzing sigmoidal aggregation kinetics showing an initial lag phase that precedes the phase of rapid growth. As the nucleation step becomes not so rate-limiting, *i.e.* as k_b increases and $v_{50} t_{50}$ decreases, the initial lag phase

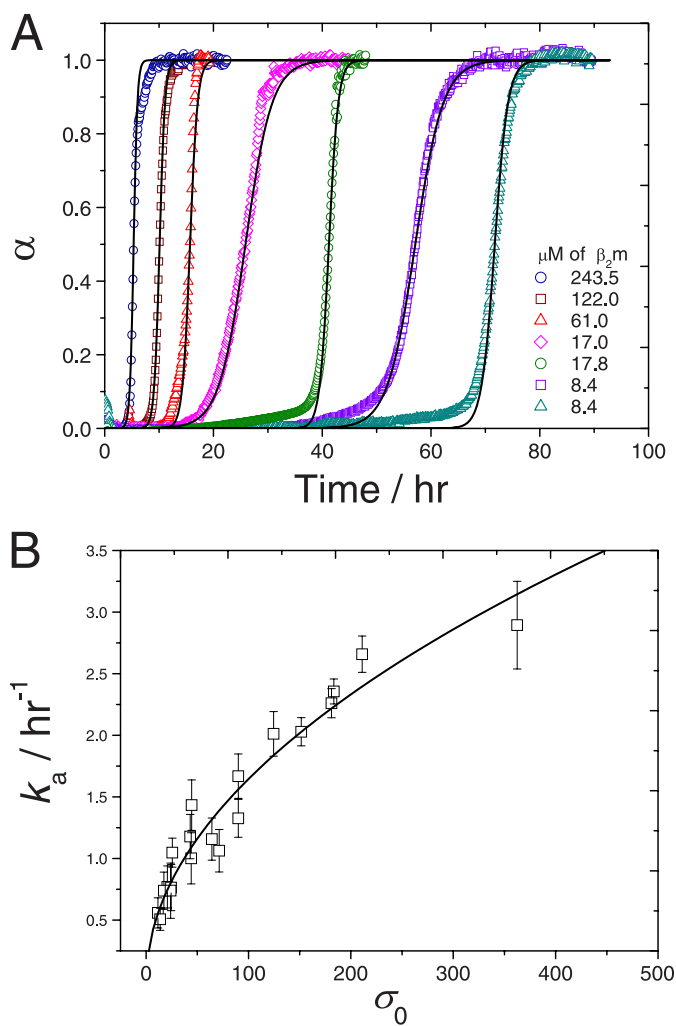


FIGURE 4. Fitting the CLM to sigmoidal aggregation kinetics measured by Xue *et al.* (15) at different β_2m concentrations. A, theoretical kinetic curves (lines) are calculated using Equation 17 and the k_a and k_b constants obtained by the simplified method described in the legend for Fig. 3. The selection of results covers very fast to very slow β_2m fibrillization kinetics. B, influence of the initial supersaturation level σ_0 on the mean k_a values (symbols) determined for different protein concentrations within a 95% confidence interval (error bars). Solid line represents a power law equation with exponent 0.503.

becomes progressively shorter until no induction time is discernible. At the same time, the shape of the amyloid fibrillization kinetics is expected to gradually change from sigmoidal to hyperbolic. This is understandable from the value of amyloid fibril conversion at the inflection point α_i , which is calculated from the condition $d^2\alpha/dt^2 = 0$ applied to Equation 13 for unseeded reactions ($\alpha_0 = 0$).

$$\alpha_i = \frac{1 - 2k_b}{2(1 - k_b)} \quad (\text{Eq. 20})$$

For low values of the nucleation-to-growth ratio, the progress of amyloid fibrillization follows a sigmoidal shape with an inflection point at $\alpha_0 = 0.5$. As k_b increases, the sigmoid curves have their inflection at lower values of α until a stage where no inflection point is visible at all. This happens for $k_b > 0.5$ and corresponds to the hyperbolic aggregation kinetics.

A good agreement between experimental and theoretical results is again observed in the case of hyperbolic aggregation

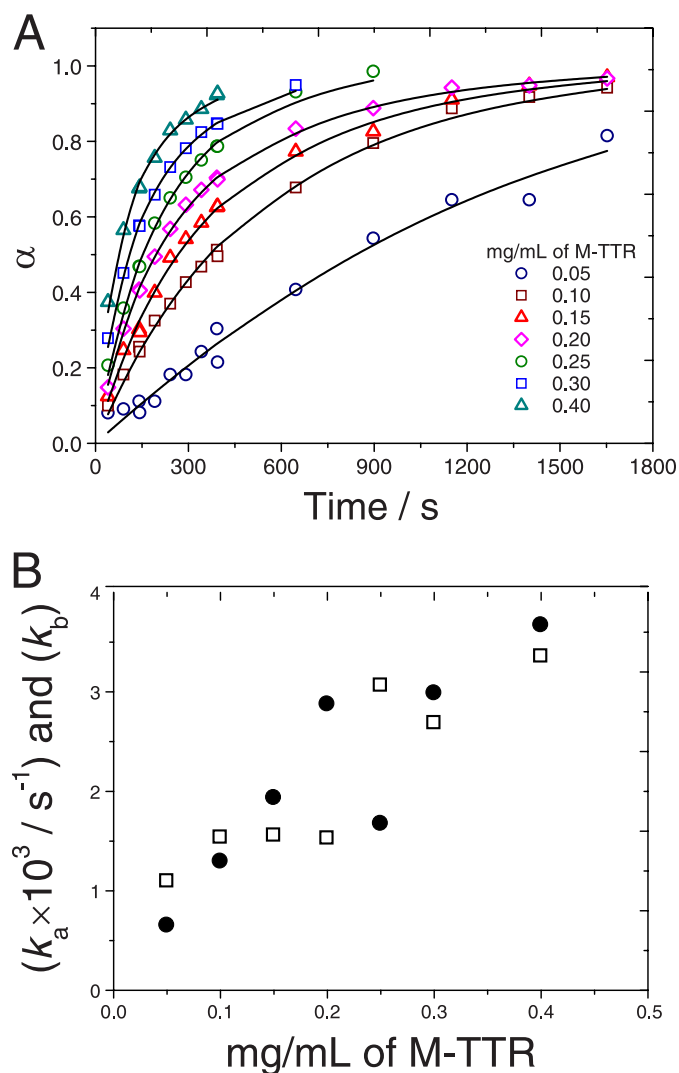


FIGURE 5. Fitting the CLM to hyperbolic aggregation kinetics measured by Hurshman *et al.* (18) at different M-TTR concentrations. *A*, symbols represent continuous fluorescence data that were digitized by us into periodic data and normalized by the end-point signal. Theoretical kinetic curves (lines) are calculated using Equation 17 and the k_a and k_b constants obtained by minimization of the squared error. *B*, influence of the initial supersaturation level σ_0 on the estimated k_a (open symbols) and k_b constants (closed symbols).

kinetics of monomeric transthyretin (M-TTR) (Fig. 5A). First estimations of k_a and k_b using the values of t_{50} and v_{50} were now fine-tuned through numerical minimization of the squared error. The parameters thus obtained are in close agreement with those obtained using the Levenberg-Marquardt algorithm of χ^2 minimization (see supplemental Table S2). Fig. 5B shows that the obtained values of k_a and k_b seem to linearly increase with the initial supersaturation level σ_0 calculated using Equation 5; a value of 0.8 $\mu\text{g}/\text{ml}$ was used for the M-TTR solubility C^* , which corresponds to the concentration of monomers in solution after 1 week of reaction time (18). Although the linear $k_a(\sigma_0)$ relationship confirms the definition of the growth rate constant given by Equation 14, the $k_b(\sigma_0)$ data suggest that in Equation 15, the average number of monomers constituting the critical nucleus \bar{n}^* increases with the initial supersaturation. This result is apparently in contradiction with the classical nucleation theory, which expects smaller critical nuclei as the

thermodynamic driving force increases (Equation 7). Additional statistically reliable nucleation data are, however, needed before making more definite conclusions about the definition of \bar{n}^* for amyloidogenesis. M-TTR and $\beta_2\text{m}$ are amyloidogenic proteins that have rather distinct fibrillization kinetics, namely in reaction speed and shape of the progress curve. The ability of CLM to describe such different aggregation mechanisms is very encouraging. Another feature clearly distinguishing the two behaviors is the role of seeding on the acceleration of amyloid aggregation. Although the addition of preformed aggregates of $\beta_2\text{m}$ has the typical effect of precluding the initial lag phase (15), in the case of M-TTR, the aggregation kinetics is not accelerated by seeding (18). The CLM again provides the rationale for these observations based on the relative importance of the nucleation step relatively to growth; the very low values of k_b estimated for $\beta_2\text{m}$ mean that amyloid nucleation is the rate-limiting step. Therefore, the initial fibrillization rate v_0 predicted by Equation 13 for $\alpha = 0$ is also very low in the absence of seeding. Even small amounts of seeds may represent mass fractions α_0 much higher than k_b , which will lead to a correspondingly high increase on the value of v_0 and to a change of fibrillization kinetics from sigmoidal to hyperbolic. On the contrary, the high values of k_b obtained for M-TTR represent fast fibrillization rates right from the beginning of the reaction. This occurs independently of the values of α_0 that are typically well below 1. Drastic differences in the value of k_b may also configure different mechanisms of M-TTR and $\beta_2\text{m}$ amyloid fibril formation; amorphous M-TTR aggregates identified by microscopic analysis (18) are likely to act as nucleation promoters (63). Instead, $\beta_2\text{m}$ fibrils had the long, straight morphology typical of low pH, low ionic strength conditions (15, 64), suggesting that elongation is the major route for fibril formation.

At this point, the CLM is confirmed as a robust two-parameter model that is able to describe very distinct protein aggregation kinetics and whose derivation is theoretically consistent and not liable to oversimplified hypothesis. As shown in supplemental Table S2 and supplemental Fig. S1, the CLM also obtained the best fitting results among the two-parameter models used to describe protein aggregation data that are not rate-limited by any of the steps. In a subsequent stage, additional mechanistic insight into the nucleation and growth steps should be gained by disclosing the meaning of the kinetic constants k_a and k_b . Our preliminary study on how these constants are affected by the initial supersaturation level seems to indicate that modifications to the classic nucleation theory are needed to determine the critical size of the amyloid nucleus. Concerning the growth step, the condition of size-dependent growth inherent to Equation 9 also deserves further discussion. This condition is not easily tested by direct observation techniques, which are known to have experimental limitations such as constrained assembly on the mica/glass surface and growth rate dispersion (41–46). An indirect, yet distinctive consequence of size-dependent growth is that fibrillization rates are affected by the total mass of fibrils present in solution but not by their number. Increased seeding efficiency obtained with fragmented (smaller) seed fibrils has, however, been observed for $\beta_2\text{m}$ (15, 52) and for yeast prions (65), which is in apparent contradiction with the size-dependent condition. Fibril break-

Protein Aggregation Described by a Two-parameter Model

age induced by different agitation intensities has also been reported to affect the end-point fluorescence signal (59, 60), which is an indication of the total amount of fibrils produced and, indirectly, of the protein solubility (Equation 6). Both types of evidences are not expected by the CLM and are presumably related with variations on the effective protein concentration due to volume-excluding effects in fibril-crowded solutions. Known as an important variable in the cellular environment, macromolecular crowding and its effects are generally associated with high concentrations of spectator molecules (66). We hypothesize that the thermodynamic concentration of protein may also be affected *in vitro* by fibril breakage as an additional source of monomer-retaining sites. Besides providing a possible explanation for masked fibrillization kinetics, changing thermodynamic conditions may also be linked to a series of unusual behaviors reported in literature such as the effects of reaction volume (67), hydrophobic surface area (68), and surfactants (60) on amyloid fibril formation. In all cases, not only the reaction rate is affected but also the reaction extent, which again supports the thermodynamic hypothesis of volume-excluding effects taking place at the fibril-solution interface. Whether the effect of fibril breakage is thermodynamic or kinetic is important to evaluate the condition of size-dependent growth and to establish the fundamental meaning of the constant k_a : (i) is it related to probabilistic interfacial collisions and the mean life time of monomers at the surface of amyloid fibrils, or (ii) should it be treated as a blind kinetic constant such as those commonly found in protein aggregation models that consider reaction-like rate equations? Either way, sufficient experimental data are available confirming a first-order dependence of the elongation rate on the fundamental variables supersaturation level and fibril mass/size, which in turn leads to a first-order dependence of k_a on the initial supersaturation level σ_0 .

The CLM opens new perspectives on the characterization and understanding of amyloid fibril kinetics. Development of new targets for amyloid disease therapeutics needs this model working together with other structural and molecular studies (55, 69) and complemented with information on the composition of toxic nonfibrillar oligomers (36, 43). CLM allows users to discern between the following mechanisms of inhibition: (i) protein solubility increase evidenced by higher values of C^* in the presence of the inhibitor, thus lowering the thermodynamic driving force for fibrillization (Equation 5); (ii) nucleation rates decrease evidenced by lower nucleation-to-growth ratios (k_b) in the presence of the inhibitor; and (iii) blocking of fibril elongation evidenced by lower kinetic constant for growth (k_a) in the presence of inhibitor. Mechanisms that require structural interaction between ligand and polypeptide, such as nucleation and/or growth inhibition, offer more guarantees to work both *in vitro* and *in vivo*. By characterizing the relative contribution of variables, the CLM is expected to be useful for scientific systematization during the development of new therapeutic strategies for amyloid diseases.

In conclusion, we propose a quantitative crystallization-like model that is able to describe the sigmoid and hyperbolic amyloid fibrillization kinetics commonly reported in literature. A simplified method is presented to determine the model parameters using Fig. 3B and the measured values of the time required

to reach 50% completion (t_{50}) and the aggregation rate at that instant (v_{50}). Further insights are provided into the nature of critically sized amyloid nucleus, the influence of diffusive limitations and fibril breakage during growth, and the role of seeding as amyloid aggregation catalyst. It is notable that the solid biophysical basis of the CLM does not compromise its final simplicity. While integrating the combined influence of seeding, nucleation, growth, and fibril breakage, Equation 17 is seen as a good approximation of the generalized underlying principle governing the kinetics of amyloid fibrillization. We expect that the CLM may be routinely used as a tool to characterize quantitatively and qualitatively new targets for amyloid disease therapeutics.

Acknowledgments—We thank Wei-Feng Xue, Sheena E. Radford, and their research team for allowing us to reproduce published experimental data in Figs. 1, 3A, and 4A. We thank Jeffery W. Kelly and the Kelly research team for allowing us to reproduce published experimental data in Figs. 1 and 5A.

REFERENCES

1. Sunde, M., Serpell, L. C., Bartlam, M., Fraser, P. E., Pepys, M. B., and Blake, C. C. (1997) Common core structure of amyloid fibrils by synchrotron x-ray diffraction. *J. Mol. Biol.* **273**, 729–739
2. Kelly, J. W. (1997) Amyloid fibril formation and protein misassembly: a structural quest for insights into amyloid and prion diseases. *Structure* **5**, 595–600
3. Greenwald, J., and Riek, R. (2010) Biology of amyloid: structure, function, and regulation. *Structure* **18**, 1244–1260
4. Morris, A. M., Watzky, M. A., and Finke, R. G. (2009) Protein aggregation kinetics, mechanism, and curve-fitting: a review of the literature. *Biochim. Biophys. Acta* **1794**, 375–397
5. Roychaudhuri, R., Yang, M., Hoshi, M. M., and Teplow, D. B. (2009) Amyloid β -protein assembly and Alzheimer disease. *J. Biol. Chem.* **284**, 4749–4753
6. Bhak, G., Choe, Y. J., and Paik, S. R. (2009) Mechanism of amyloidogenesis: nucleation-dependent fibrillation versus double-concerted fibrillation. *BMB Rep.* **42**, 541–551
7. Knowles, T. P., Waudby, C. A., Devlin, G. L., Cohen, S. I., Aguzzi, A., Vendruscolo, M., Terentjev, E. M., Welland, M. E., and Dobson, C. M. (2009) An analytical solution to the kinetics of breakable filament assembly. *Science* **326**, 1533–1537
8. Nilsson, M. R. (2004) Techniques to study amyloid fibril formation *in vitro*. *Methods* **34**, 151–160
9. Bondos, S. E. (2006) Methods for measuring protein aggregation. *Curr. Anal. Chem.* **2**, 157–170
10. Harper, J. D., and Lansbury, P. T. (1997) Models of amyloid seeding in Alzheimer disease and scrapie: mechanistic truths and physiological consequences of the time-dependent solubility of amyloid proteins. *Annu. Rev. Biochem.* **66**, 385–407
11. Frieden, C. (2007) Protein aggregation processes: in search of the mechanism. *Protein Sci.* **16**, 2334–2344
12. Naiki, H., Higuchi, K., Hosokawa, M., and Takeda, T. (1989) Fluorometric determination of amyloid fibrils *in vitro* using the fluorescent dye, thioflavin T1. *Anal. Biochem.* **177**, 244–249
13. Jarrett, J. T., and Lansbury, P. T., Jr. (1992) Amyloid fibril formation requires a chemically discriminating nucleation event: studies of an amyloidogenic sequence from the bacterial protein OsmB. *Biochemistry* **31**, 12345–12352
14. Knowles, T. P., Shu, W., Devlin, G. L., Meehan, S., Auer, S., Dobson, C. M., and Welland, M. E. (2007) Kinetics and thermodynamics of amyloid formation from direct measurements of fluctuations in fibril mass. *Proc. Natl. Acad. Sci. U.S.A.* **104**, 10016–10021
15. Xue, W. F., Homans, S. W., and Radford, S. E. (2008) Systematic analysis of nucleation-dependent polymerization reveals new insights into the mech-

- anism of amyloid self-assembly. *Proc. Natl. Acad. Sci. U.S.A.* **105**, 8926–8931
16. Naiki, H., Hasegawa, K., Yamaguchi, I., Nakamura, H., Gejyo, F., and Nakakuki, K. (1998) Apolipoprotein E and antioxidants have different mechanisms of inhibiting Alzheimer β -amyloid fibril formation *in vitro*. *Biochemistry* **37**, 17882–17889
 17. Jarrett, J. T., and Lansbury, P. T., Jr. (1993) Seeding “one-dimensional crystallization” of amyloid: a pathogenic mechanism in Alzheimer disease and scrapie? *Cell* **73**, 1055–1058
 18. Hurshman, A. R., White, J. T., Powers, E. T., and Kelly, J. W. (2004) Transthyretin aggregation under partially denaturing conditions is a downhill polymerization. *Biochemistry* **43**, 7365–7381
 19. Naiki, H., Gejyo, F., and Nakakuki, K. (1997) Concentration-dependent inhibitory effects of apolipoprotein E on Alzheimer β -amyloid fibril formation *in vitro*. *Biochemistry* **36**, 6243–6250
 20. Morris, A. M., Watzky, M. A., Agar, J. N., and Finke, R. G. (2008) Fitting neurological protein aggregation kinetic data via a two-step, minimal/“Ockham’s razor” model: the Finke-Watzky mechanism of nucleation followed by autocatalytic surface growth. *Biochemistry* **47**, 2413–2427
 21. Schmidt, H., Madsen, M. F., Danø, S., and Cedersund, G. (2008) Complexity reduction of biochemical rate expressions. *Bioinformatics* **24**, 848–854
 22. Bernacki, J. P., and Murphy, R. M. (2009) Model discrimination and mechanistic interpretation of kinetic data in protein aggregation studies. *Biophys. J.* **96**, 2871–2887
 23. Watzky, M. A., and Finke, R. G. (1997) Transition metal nanocluster formation kinetic and mechanistic studies: a new mechanism when hydrogen is the reductant: slow, continuous nucleation and fast autocatalytic surface growth. *J. Am. Chem. Soc.* **119**, 10382–10400
 24. Kamihira, M., Naito, A., Tuzi, S., Nosaka, A. Y., and Saitō, H. (2000) Conformational transitions and fibrillation mechanism of human calcitonin as studied by high-resolution solid-state ^{13}C NMR. *Protein Sci.* **9**, 867–877
 25. Fernández, C. O., Hoyer, W., Zweckstetter, M., Jares-Erijman, E. A., Subramaniam, V., Griesinger, C., and Jovin, T. M. (2004) NMR of α -synuclein-polyamine complexes elucidates the mechanism and kinetics of induced aggregation. *EMBO J.* **23**, 2039–2046
 26. Ferrone, F. (1999) Analysis of protein aggregation kinetics. *Methods Enzymol.* **309**, 256–274
 27. Watzky, M. A., Morris, A. M., Ross, E. D., and Finke, R. G. (2008) Fitting yeast and mammalian prion aggregation kinetic data with the Finke-Watzky two-step model of nucleation and autocatalytic growth. *Biochemistry* **47**, 10790–10800
 28. Sluzky, V., Tamada, J. A., Klibanov, A. M., and Langer, R. (1991) Kinetics of insulin aggregation in aqueous solutions upon agitation in the presence of hydrophobic surfaces. *Proc. Natl. Acad. Sci. U.S.A.* **88**, 9377–9381
 29. O’Nuallain, B., Shivaprasad, S., Kheterpal, I., and Wetzel, R. (2005) Thermodynamics of $\text{A}\beta(1-40)$ amyloid fibril elongation. *Biochemistry* **44**, 12709–12718
 30. Hasegawa, K., Ono, K., Yamada, M., and Naiki, H. (2002) Kinetic modeling and determination of reaction constants of Alzheimer β -amyloid fibril extension and dissociation using surface plasmon resonance. *Biochemistry* **41**, 13489–13498
 31. Auer, S., and Kashchiev, D. (2010) Insight into the correlation between lag time and aggregation rate in the kinetics of protein aggregation. *Proteins* **78**, 2412–2416
 32. Markov, I. V. (2003) *Crystal Growth for Beginners*, 2nd Ed., World Scientific Publishing, Singapore
 33. Minton, A. P. (2000) Implications of macromolecular crowding for protein assembly. *Curr. Opin. Struct. Biol.* **10**, 34–39
 34. Chiti, F., and Dobson, C. M. (2009) Amyloid formation by globular proteins under native conditions. *Nat. Chem. Biol.* **5**, 15–22
 35. Stöhr, J., Weinmann, N., Wille, H., Kaimann, T., Nagel-Steger, L., Birkmann, E., Panza, G., Prusiner, S. B., Eigen, M., and Riesner, D. (2008) Mechanisms of prion protein assembly into amyloid. *Proc. Natl. Acad. Sci. U.S.A.* **105**, 2409–2414
 36. Bhak, G., Lee, J. H., Hahn, J. S., and Paik, S. R. (2009) Granular assembly of α -synuclein leading to the accelerated amyloid fibril formation with shear stress. *PLoS ONE* **4**, e4177
 37. Kashchiev, D. (2000) *Nucleation: Basic Theory with Applications*, Butterworth-Heinemann, Oxford
 38. Kashchiev, D., and Auer, S. (2010) Nucleation of amyloid fibrils. *J. Chem. Phys.* **132**, 215101
 39. Zhang, T. H., and Liu, X. Y. (2009) Nucleation: what happens at the initial stage? *Angew. Chem. Int. Ed. Engl.* **48**, 1308–1312
 40. Padrick, S. B., and Miranker, A. D. (2002) Islet amyloid: phase partitioning and secondary nucleation are central to the mechanism of fibrillogenesis. *Biochemistry* **41**, 4694–4703
 41. Heldt, C. L., Zhang, S., and Belfort, G. (2011) Asymmetric amyloid fibril elongation: a new perspective on a symmetric world. *Proteins* **79**, 92–98
 42. Ban, T., and Goto, Y. (2006) Direct observation of amyloid growth monitored by total internal reflection fluorescence microscopy. *Methods Enzymol.* **413**, 91–102
 43. Collins, S. R., Douglass, A., Vale, R. D., and Weissman, J. S. (2004) Mechanism of prion propagation: amyloid growth occurs by monomer addition. *PLoS Biol.* **2**, e321
 44. Patil, S. M., Mehta, A., Jha, S., and Alexandrescu, A. T. (2011) Heterogeneous amylin fibril growth mechanisms imaged by total internal reflection fluorescence microscopy. *Biochemistry* **50**, 2808–2819
 45. Scheibel, T., Kowal, A. S., Bloom, J. D., and Lindquist, S. L. (2001) Bidirectional amyloid fiber growth for a yeast prion determinant. *Curr. Biol.* **11**, 366–369
 46. Goldsbury, C., Kistler, J., Aebi, U., Arvinte, T., and Cooper, G. J. (1999) Watching amyloid fibrils grow by time-lapse atomic force microscopy. *J. Mol. Biol.* **285**, 33–39
 47. Ionescu-Zanetti, C., Khurana, R., Gillespie, J. R., Petrick, J. S., Trabachino, L. C., Minert, L. J., Carter, S. A., and Fink, A. L. (1999) Monitoring the assembly of Ig light-chain amyloid fibrils by atomic force microscopy. *Proc. Natl. Acad. Sci. U.S.A.* **96**, 13175–13179
 48. Ruschak, A. M., and Miranker, A. D. (2007) Fiber-dependent amyloid formation as catalysis of an existing reaction pathway. *Proc. Natl. Acad. Sci. U.S.A.* **104**, 12341–12346
 49. Martins, P. M., and Rocha, F. (2007) Characterization of crystal growth using a spiral nucleation model. *Surf. Sci.* **601**, 3400–3408
 50. Martins, P. M., and Rocha, F. (2007) New developments on size-dependent growth applied to the crystallization of sucrose. *Surf. Sci.* **601**, 5466–5472
 51. Martins, P. M., and Rocha, F. A. (2008) Kinetic studies on the influence of temperature and growth rate history on crystal growth. *Cryst. Res. Technol.* **43**, 1258–1267
 52. Chatani, E., Ohnishi, R., Konuma, T., Sakurai, K., Naiki, H., and Goto, Y. (2010) Pre-steady-state kinetic analysis of the elongation of amyloid fibrils of β_2 -microglobulin with tryptophan mutagenesis. *J. Mol. Biol.* **400**, 1057–1066
 53. Konuma, T., Chatani, E., Yagi, M., Sakurai, K., Ikegami, T., Naiki, H., and Goto, Y. (2011) Kinetic intermediates of β_2 -microglobulin fibril elongation probed by pulse-labeling H/D exchange combined with NMR analysis. *J. Mol. Biol.* **405**, 851–862
 54. Jiménez, J. L., Nettleton, E. J., Bouchard, M., Robinson, C. V., Dobson, C. M., and Saibil, H. R. (2002) The protofilament structure of insulin amyloid fibrils. *Proc. Natl. Acad. Sci. U.S.A.* **99**, 9196–9201
 55. Santoso, A., Chien, P., Osheroich, L. Z., and Weissman, J. S. (2000) Molecular basis of a yeast prion species barrier. *Cell* **100**, 277–288
 56. Smith, J. F., Knowles, T. P., Dobson, C. M., Macphée, C. E., and Welland, M. E. (2006) Characterization of the nanoscale properties of individual amyloid fibrils. *Proc. Natl. Acad. Sci. U.S.A.* **103**, 15806–15811
 57. Xue, W. F., Hellewell, A. L., Gosal, W. S., Homans, S. W., Hewitt, E. W., and Radford, S. E. (2009) Fibril fragmentation enhances amyloid cytotoxicity. *J. Biol. Chem.* **284**, 34272–34282
 58. Ohhashi, Y., Kihara, M., Naiki, H., and Goto, Y. (2005) Ultrasonication-induced amyloid fibril formation of β_2 -microglobulin. *J. Biol. Chem.* **280**, 32843–32848
 59. Kim, H. J., Chatani, E., Goto, Y., and Paik, S. R. (2007) Seed-dependent accelerated fibrillation of α -synuclein induced by periodic ultrasonication treatment. *J. Microbiol. Biotechnol.* **17**, 2027–2032
 60. Giehm, L., and Otzen, D. E. (2010) Strategies to increase the reproducibility of protein fibrillization in plate reader assays. *Anal. Biochem.* **400**, 270–281
 61. Fändrich, M. (2007) Absolute correlation between lag time and growth

Protein Aggregation Described by a Two-parameter Model

- rate in the spontaneous formation of several amyloid-like aggregates and fibrils. *J. Mol. Biol.* **365**, 1266–1270
62. Sasahara, K., Yagi, H., Sakai, M., Naiki, H., and Goto, Y. (2008) Amyloid nucleation triggered by agitation of β_2 -microglobulin under acidic and neutral pH conditions. *Biochemistry* **47**, 2650–2660
63. Rochet, J. C., and Lansbury, P. T., Jr. (2000) Amyloid fibrillogenesis: themes and variations. *Curr. Opin. Struct. Biol.* **10**, 60–68
64. Radford, S. E., Gosal, W. S., and Platt, G. W. (2005) Towards an understanding of the structural molecular mechanism of β_2 -microglobulin amyloid formation *in vitro*. *Biochim. Biophys. Acta* **1753**, 51–63
65. Tanaka, M., Collins, S. R., Toyama, B. H., and Weissman, J. S. (2006) The physical basis of how prion conformations determine strain phenotypes. *Nature* **442**, 585–589
66. White, D. A., Buell, A. K., Knowles, T. P., Welland, M. E., and Dobson, C. M. (2010) Protein aggregation in crowded environments. *J. Am. Chem. Soc.* **132**, 5170–5175
67. Baskakov, I. V., and Bocharova, O. V. (2005) *In vitro* conversion of mammalian prion protein into amyloid fibrils displays unusual features. *Biochemistry* **44**, 2339–2348
68. Pronchik, J., He, X., Giurleo, J. T., and Talaga, D. S. (2010) *In vitro* formation of amyloid from α -synuclein is dominated by reactions at hydrophobic interfaces. *J. Am. Chem. Soc.* **132**, 9797–9803
69. Toyama, B. H., Kelly, M. J., Gross, J. D., and Weissman, J. S. (2007) The structural basis of yeast prion strain variants. *Nature* **449**, 233–237